Hyperspectral Reconstruction from RGB Images for Vein Visualization

Neha Sharma
School of Computing Science
Simon Fraser University
Burnaby, BC, Canada

Mohamed Hefeeda
School of Computing Science
Simon Fraser University
Burnaby, BC, Canada

ABSTRACT

A hyperspectral camera captures a scene in many frequency bands across the spectrum, providing rich information and facilitating numerous applications. The potential of hyperspectral imaging has been established for decades. However, to date hyperspectral imaging has only seen success in specialized and large-scale industrial and military applications. This is mainly due to the high cost of hyperspectral cameras (upwards of $20K) and the complexity of the acquisition system which makes the technology out of reach for many commercial and end-user applications. In this paper, we propose a deep learning based approach to convert RGB image sequences taken by regular cameras to (partial) hyperspectral images. This can enable, for example, low-cost mobile phones to leverage the characteristics of hyperspectral images in implementing novel applications. We show the benefits of the conversion model by designing a vein localization and visualization application that traditionally uses hyperspectral images. Our application uses only RGB images and produces accurate results. Vein visualization is important for point-of-care medical applications. We collected hyperspectral data to validate the proposed conversion model. Experimental results demonstrate that the proposed method is promising and can bring some of the benefits of expensive hyperspectral cameras to the low-cost and pervasive RGB cameras, enabling many new applications and enhancing the performance of others. We also evaluate the vein visualization application and show its accuracy.

CCS CONCEPTS

• **Computing methodologies** → **Hyperspectral imaging**.

KEYWORDS

hyperspectral imaging, vein visualization

ACM Reference Format:
Neha Sharma and Mohamed Hefeeda. 2020. Hyperspectral Reconstruction from RGB Images for Vein Visualization. In *11th ACM Multimedia Systems Conference (MMSys'20), June 8–11, 2020, Istanbul, Turkey.* ACM, New York, NY, USA, 11 pages. https://doi.org/10.1145/3339825.3391861

MMSys'20, June 8–11, 2020, Istanbul, Turkey

ACM ISBN 978-1-4503-6845-2/20/06…$15.00
https://doi.org/10.1145/3339825.3391861

1 INTRODUCTION

Vein visualization is important for various point-of-care applications. One important application is needle insertion [38, 39], which is widely used for blood sample collection and anesthesia injection during major surgeries. Vein visualization is also gaining popularity in forensic applications [8]. Although various biometric systems are available for commercial and government applications, in some forensic cases, recognizing skin texture and identifying vein patterns may be the only option left to identify the culprit. In majority of cases including identifying terrorists, gun men, rioters wearing masks in violent crime scenes, and pedophiles in child sexual offense images [35], the traditional biometric attributes (e.g., faces and tattoos) are not always available because criminals hide them to avoid identification. Thus, vein pattern matching is used to narrow down the list of suspects.

The most common method used to locate veins by doctors and clinicians is manual, which results in low rates of successful needle insertion, especially for obese patients and infants [23]. Insertion failure may cause severe health conditions such as allergies, blood clotting and even vein damage [33]. Ultrasound imaging is a promising technology for improving the success rate of vascular accessing. This technology visualizes the location of veins at various depths and significantly decreases the failure rate, particularly when used by less experienced clinicians. However, ultrasound imaging is not widely available due to the high cost and large processing time. Another important technology used to localize veins is the infrared laser excitation, which is used to differentiate veins from other soft tissues based on their spectroscopic optical absorption coefficients [39].

Hyperspectral images contain information in wide range of the spectrum including the infrared range as opposed to regular RGB images which contain information only in the visible spectrum. The complete spectral information can only be captured using expensive hyperspectral cameras having bulky and complex hardware. The captured images are called hyperspectral images, and they contain rich information even beyond the human vision. A simple illustration of hyperspectral imaging is shown in Figure 1, which shows the spatial x, y domain as well as the spectral λ domain. For each value of λ, the scene is captured in a different wavelength bands across the electromagnetic spectrum, and thus different information is revealed. The captured data is referred to as a hyperspectral data cube. Spectral information captured in the data cube can be used to produce a spectral signature, which can be used to identify different materials in the scene. For example, signal values in certain wavelength bands corresponding to the presence of soil in a scene differ from the presence of rocks or water. Using a similar concept, hyperspectral images can provide effective vein visualization.

Currently, commercially available hyperspectral cameras can capture more than 200 bands, and thus provide large amounts of high-dimensional data. Hyperspectral imaging is useful in many civil, environmental and military applications such as agricultural research, forest monitoring, and remote sensing. Initially, hyperspectral imaging was implemented on satellites and airborne platforms but recent technological advances for capturing and processing devices have made it useful in numerous applications such as material identification, art authentication, medical diagnosis, analysis of crime scene details, document image analysis including signature extraction, ink or document aging, information retrieval from historical document images, and food quality control.

Hyperspectral images are expensive to capture and require specialized hardware that is not readily accessible by most users. Digital and smartphone cameras, on the other hand, are significantly cheaper and can easily be used in everyday life. These cameras use filters on their sensors to convert the incoming light into three color channels (Red, Green, and Blue). These filters result in a loss of the other spectral information within the visible range. But, many applications require information in some target spectral range based on the optical properties of the materials used in the application. Also, the target spectral range will vary based on the application. Thus, the motivation of this work is to develop a framework which can be used to design various applications harnessing hyperspectral imaging characteristics. We propose a deep learning based method to reconstruct an object's spectral reflectance from a single RGB image captured by a regular camera, which can be used in many applications.

The contributions of this paper are summarized as follows:

- We propose a data-driven method to reconstruct hyperspectral images from RGB images. Our method is the first to produce hyperspectral recovery from RGB beyond the visible spectrum.
- We show the potential of our method by developing a human vein visualization application that uses only regular RGB images.
- We conduct a subjective study to collect dataset of hyperspectral images to evaluate the performance of the proposed vein visualization method. The subjective study was approved by the Research Ethics Board of our university. This is the first dataset in this domain and we make it available for other researchers at [9, 10].
- We conduct experiments to show the accuracy of our RGB to hyperspectral conversion method as well as the accuracy of the vein visualization application.

The rest of this paper is organized as follows. We summarize the related work in Section 2. We present the proposed method in Section 3. We present our experimental evaluation in Section 4. We conclude the paper in Section 5.

2 RELATED WORK

Vein Visualization. Multiple medical devices, e.g., [13, 37], work in the infrared range to produce vein visualization. These devices illuminate the target scene with infrared light, which penetrates deep inside the skin and produce vein localization map [24]. These devices are expensive and are not suitable for point-of-care applications. There are methods to produce low cost infrared vein visualization [30]. Most of the methods use an infrared light source with a traditional RGB camera sensor to acquire vein-enhanced images. Ayoub et al. [5] use 850nm and 940nm wavelength light sources along with a Nikon D810 camera to capture veins. Goel et al. [15] design an imaging system having 17 LEDs in the wavelength range $450 - 990nm$ with a CMOS camera sensor. All these low cost image acquisition systems require special hardware configurations, which is not suitable for most practical cases. Software-based approaches for vein visualization have also been considered in the literature. For example, Song et al. [32] perform multispectral vein visualization from RGB images using Wiener estimation. They estimate the reflectance spectrum matrix for a GALAXY Note 2 camera using spectrometer in the wavelength range $380 - 780nm$. Their method requires calibration and estimation matrix calculation for each smartphone device using a spectrometer, which is not practical for wide deployment.

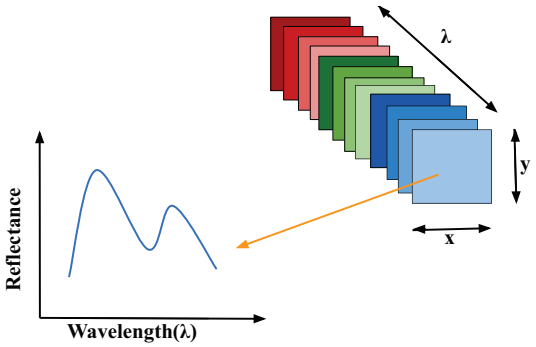

Figure 1: Hyperspectral data cube with spectral signature.

Hyperspectral Reconstruction from RGB. Hyperspectral imaging has proved to be useful in several applications from agriculture and food processing to medical diagnosis and surveillance [2, 18]. Hyperspectral cameras are, however, expensive and bulky, which makes them out of reach for most end users. To overcome this barrier, there is a variety of approaches to get hyperspectral images without using a hyperspectral camera. Some methods use commercial RGB cameras and reconstruct the reflectance spectrum. Oh et al. [29] exploited the different spectral sensitivities of multiple camera sensors to reconstruct the visible spectrum. Other methods use add-on devices such as color filters and reflectors [20, 34]. Also, there are methods that use a single RGB image to reconstruct the spectrum, such as principal component analysis (PCA) [1, 7], interpolation [25], and weighted canonical correlation regression [12]. Recently, training-based approaches [4] for spectral reconstruction have been considered. Nguyen et al. [27] consider a non-linear mapping strategy for modeling the camera-specific RGB values and scene reflectance spectra. They use a radial basis function network for modeling the mapping. Xiong et al. [22, 31, 36] present a deep learning framework to recover hyperspectral images from spectrally undersampled projections.

All the methods explained above produce sparse reconstruction only in *visible* range of the spectrum. That is, all prior methods

work in the spectral range $400 - 700nm$. In contrast, we present a deep learning method that produces reconstruction outside the visible range, which adds more value to different applications. In addition, unlike prior conversion methods, our method handles different illumination conditions, which is a desirable feature for practical uses.

3 PROBLEM STATEMENT AND PROPOSED METHOD

3.1 Problem Definition

As mentioned in Section 1, high-quality vein visualization is clinically important for various point-of-care applications. The main function of veins is to transport oxygen rich (oxyhemoglobin) blood and carbon dioxide rich (deoxyhemoglobin) blood throughout the body. Thus, the major component present in veins is hemoglobin. Hemoglobin absorbs most of the infrared light, distinguishing veins from the skin.

Hyperspectral cameras can easily show veins using information in the infrared range. A hyperspectral image acquisition system contains an illumination source which illuminates the target scene. The light reflected is then captured by the imaging system. The imaging system digitizes the incoming signal and captures the information in m bands, throughout the electromagnetic spectrum as shown in Figure 2. Practical hyperspectral applications utilize only a small subset of the bands. The bands useful for vein visualization are illustrated in Figure 2, which are located in the Near-Infrared (NIR) range. Thus, in this work, we focus on designing an application-specific RGB to hyperspectral conversion method, in which we convert an RGB image to a few carefully selected bands that are the most useful for the considered application.

In particular, our problem is to reconstruct a target n number of bands from RGB images. The problem can be defined as follows:

$$I_{HS} = f(I_{RGB}), \tag{1}$$

where I_{HS} is the reconstructed hyperspectral image containing n target bands $(b_1, b_2, ..., b_n)$ and f is the transformation function which takes an RGB image, I_{RGB}, as input. The goal is to estimate the transformation function f as accurately as possible.

Our problem is general and can be customized for various hyperspectral applications. The specific bands to be estimated are first identified based on the application needs. Then, our deep learning model is fine-tuned to reconstruct these bands.

In the following subsection, we describe the proposed RGB to hyperspectral conversion method. in Section 3.3, we describe the customization of our method to human vein visualization.

3.2 RGB to Hyperspectral Conversion

We propose a deep learning approach to reconstruct hyperspectral image having n bands, $b_1, b_2, \ldots, b_n$, across the electromagnetic spectrum from a given RGB image with 3 bands: Red (R), Green (G), and Blue (B). The deep learning model is configurable based on the number of bands required for the considered application. Our model is different from previous ones in the literature: it converts RGB images to specific n bands instead of trying to estimate the entire visible spectrum as in [3, 4, 27]. Our approach produces higher accuracy for the considered application as well as make the model less complex.

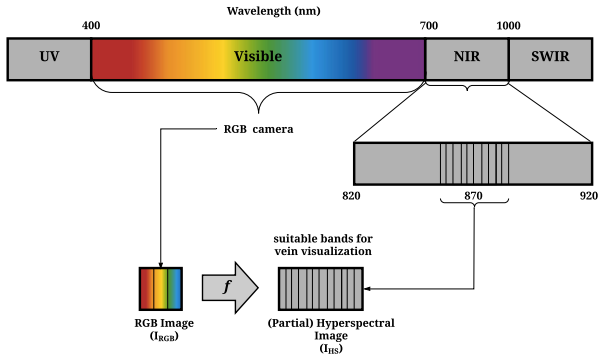

Figure 2: Hyperspectral cameras operate in a wide range of the spectrum including ultraviolet (UV), visible, near infrared (NIR) and short wavelength infrared (SWIR). The goal of this paper is to take RGB signals in the visible range and convert them to specific NIR bands using a deep learning model to localize human veins.

Converting RGB images to hyperspectral images introduces challenges that do not exist in common image-to-image translation works in the literature. The first challenge is the lack of paired RGB-hyperspectral datasets. We address this challenge by collecting our own dataset using a commercial hyperspectral camera and make the dataset available [10]. Second, a hyperspectral image has many bands, and since these bands are captured at different wavelengths, pixels in various bands have significantly different luminance levels, which could impact the performance of the neural network. Figure 3 shows four different bands produced by our hyperspectral camera capturing the same scene. Notice the different luminance (darkness) values of pixels in different bands. We mitigate this problem by designing a new loss function for the neural network.

The third and more difficult challenge in converting RGB images to hyperspectral ones is the effect of external illumination. Specifically, the mapping between an RGB image to hyperspectral bands depends heavily on the scene illumination. Thus, producing robust neural network models requires training with huge datasets covering different illuminations that occur in real scenarios. Capturing such paired RGB-hyperspectral imaging datasets is not practical, given the wide variety of illumination scenarios and the high cost of hyperspectral cameras. We address this challenge by using a white balancing approach to neutralize the effect of illumination on the neural network.

We present the details of our approach in the following.

Neural Network Design. The proposed convolutional neural network model is designed to spectrally upsample the RGB image to n bands in the specific part of the electromagnetic spectrum. Our model architecture is depicted in Figure 4, which is based on the model in [31]. The feature extraction from the three input RGB bands is done by a convolution layer, followed by 10 residual blocks [16] for feature mapping along with the global residual learning.

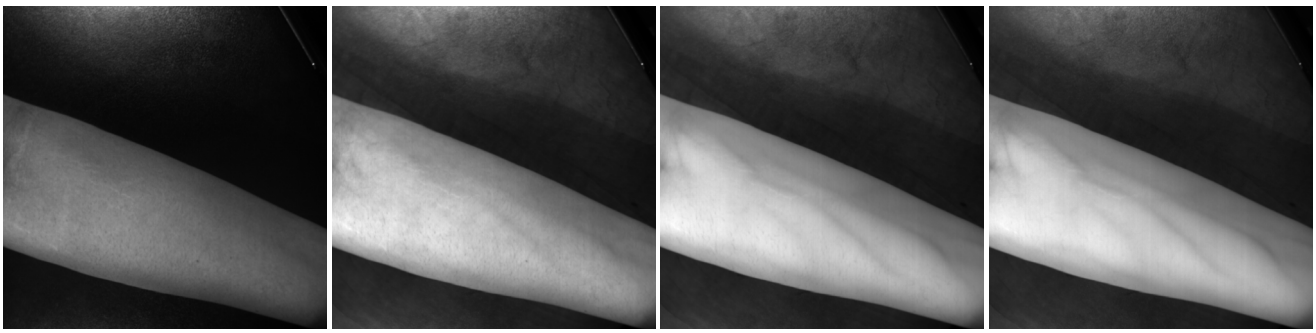

Figure 3: Luminance levels in different hyperspectral bands at different wavelength. The figure shows grayscale renderings of four bands at 450nm (first) and 600nm (second) in the visible range, and 750nm (third) and 900nm (last) in the infrared range.

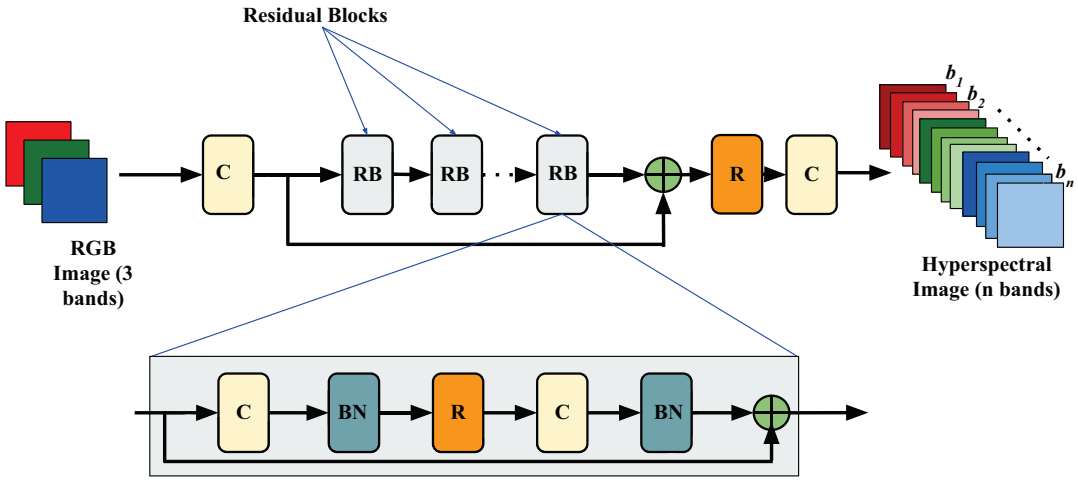

Figure 4: Network architecture of the proposed model. "C" denotes convolution, "R" and "BN" represent the ReLU activation function and Batch Normalization, respectively. "RB" denotes residual block, which is expanded in the lower part of the figure.

Each residual block is defined as:

$$y = F(x, W_k) + x, \tag{2}$$

where x and y are the input and output of the block, W_k represents the weight matrix of the k^{th} block, and $F(\cdot)$ denotes the residual mapping to be learned which consists of two convolutions separated by one ReLU layer [26]. We add batch normalization [17] after each convolution layer in the residual block for faster training and better performance. The addition is element-wise and performed by a shortcut connection. After feature learning, the reconstruction is done by one ReLU, followed by one convolution in the end. The filter size of convolution is uniformly set to 3×3 in the entire architecture.

Loss function. Deep learning methods generally adopt the mean square error (MSE) as the loss function [11, 19] for image restoration during training, which has also been used in previous hyperspectral reconstruction methods [3, 36]. However, as discussed above, in case of hyperspectral images, the luminance level varies significantly across different bands as shown in Figure 3. Thus, the MSE loss can introduce a bias towards the bands with higher luminance levels. To address this issue, we use the mean relative absolute error (MRAE) as the loss function for training our model. The mean relative absolute error is defined as:

$$MRAE = \frac{1}{N} \sum_{i,b} | \, (I^R_{i,b} - I^G_{i,b}) / I^G_{i,b} \, |, \tag{3}$$

where $I^R_{i,b}$ and $I^G_{i,b}$ denote the i^{th} pixel in band b of the reconstructed and ground truth hyperspectral images, respectively, and N is the total number of pixels.

Handling Various Illuminations. The main challenge in spectral reconstruction is encountered when images are captured in different illuminations, which can be explained as follows. Consider two different spectral reflectances $R_1(\lambda)$ and $R_2(\lambda)$ captured in two different spectral illuminations $L_1(\lambda)$ and $L_2(\lambda)$, respectively over a given wavelength λ. Then, it is possible that under a certain observer $O_{RGB}(\lambda)$ both reflectances produce the same RGB image, which can be expressed as:

$$\int_\lambda L_1(\lambda) R_1(\lambda) O_{RGB}(\lambda) = \int_\lambda L_2(\lambda) R_2(\lambda) O_{RGB}(\lambda).$$

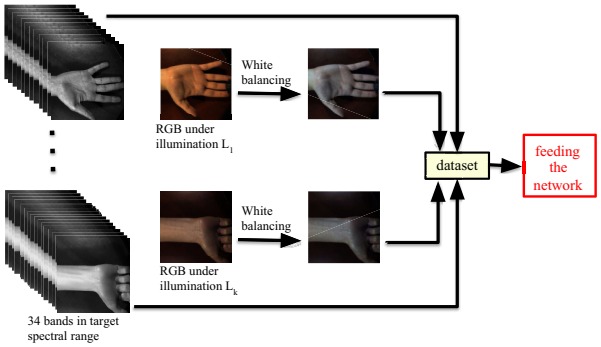

Figure 5: Handling different illumination conditions using white balancing step in the training process.

We handle different illumination conditions by normalizing the RGB images using a white-balancing method before they are used for training the network, as illustrated in Figure 5. For the white-balancing step, we use the shades of grey (SoG) method. As proposed in [14], the Gray World and the Max-RGB algorithm are two instances of a more general color constancy algorithm based on the Minkowski norm. The Minkowski-norm provides the normalized result of the estimated illumination vector. It computes a weighted average of the pixel values, assigning larger weights to pixels with larger intensities. The best performance for SoG is given by Minkowski norm of order 5. We selected SoG due to its simplicity, low computational requirement and its effectiveness over various datasets.

The white balanced image $I_c^{'}$ corresponding to the RGB image I_c is obtained by using the following expression:

$$I_c^{'} = diag(\frac{1}{t_r}, \frac{1}{t_g}, \frac{1}{t_b})I_c, \tag{4}$$

where $\mathbf{t} = [t_r, t_g, t_b]$ is the white balancing vector obtained by the chosen white balancing algorithm (SoG).

3.3 Customization to Vein Visualization

As mentioned in the previous subsection, the proposed RGB to hyperspectral conversion method is general and can work for different applications. In this subsection, we present a concrete example on human vein visualization.

Identifying Relevant Hyperspectral Bands. The first step is to discover the relevant hyperspectral band(s) useful for vein visualization. To identify these bands, we captured and visually inspected several hyperspectral images using our hyperspectral camera which produces 204 bands covering the spectrum between $400 - 1000nm$. Our inspection indicates that bands in the spectral range $820 - 920nm$ provide the best vein visualization. This is inline with the fact that most medical devices for vein visualization illuminate the target scene with a near infrared light source with a wavelength of $850nm$, because this wavelength penetrates deep inside the skin [5, 30]. We show in Figure 6 renderings of four samples at $850nm$ in the infrared range captured by our hyperspectral camera. Veins are clearly visible in the samples. Thus, for vein visualization, a single band in the spectral range $820 - 920nm$ is sufficient. In our design, we use the $850nm$ band. That is, we convert RGB images to images in the $850nm$ band, which is in the near infrared range. Furthermore, since bands close to the $850nm$ provide somewhat similar information, we use these bands as well in the training of our models. That is, for each sample taken from a human subject, we pair the RGB image with each band in the spectral range $820 - 920nm$ and use the resulting pairs in the training. Our hyperspectral camera produces 34 bands in the $820 - 920nm$ range. This simple idea allowed us to generate more data to train our models and reduce the potential of over fitting.

Enhancing the Produced Images. After reconstructing the $850nm$ band from RGB, we postprocess the produced image to improve vein visualization. Specifically, we perform image enhancement to produce better contrast between superficial veins and human skin. We use two types of image enhancement methods explained as follows:

- *Contrast Limited Adaptive Histogram Equalization [6] (CLAHE)*: CLAHE is an improvement over the standard Histogram Equalization (HE) method. CLAHE first partitions the image into a number of non-overlapping contextual regions. A histogram is calculated and constructed separately according to the size of contextual regions. After that, a threshold value is determined for clipping histograms. The clipped pixels are then distributed back to the clipped histogram. Finally, the gray level mappings are combined using bilinear interpolation in order to produce the final enhanced image.
- *Homomorphic Filtering [28](HF)*: Homomorphic filtering is generally used to remove multiplicative noise. It enhances images by increasing the high frequency components and decreasing the low frequency components. It first applies a logarithm function on the input image. After that, the low frequency component is suppressed in the Fourier domain. Finally, the output image is produced by applying the inverse logarithm function.

4 EXPERIMENTAL EVALUATION

This section describes the experiments performed to qualitatively and quantitatively assess the performance of the proposed method to convert RGB images to hyperspectral ones and its application to vein visualization for human subjects.

4.1 Experimental Setup

Image Acquisition Setup. The image acquisition setup is shown in Figure 7. It consists of an experimental table, a hyperspectral camera mounted on a tripod stand facing towards the experimental table, 2 halogen lamps illuminating the scene towards the capturing area, and a chair for the human subject to sit on while extending his/her hand/arm to the capturing area on the table.

We used the Specim IQ hyperspectral camera, which is a line scanning camera with a built-in scanner. This camera works in the $400 - 1000nm$ spectral range with $\sim 3nm$ spectral resolution providing 204 bands. This camera operates by chargeable batteries and it has a memory card to save the captured data. It also has a mini display to help in focusing and adjusting the camera lens before capturing. Captured images are later transferred to a workstation

Figure 6: Band analysis to identify relevant bands for vein visualization. The figure shows grayscale renderings of four samples at $850nm$ in the infrared range.

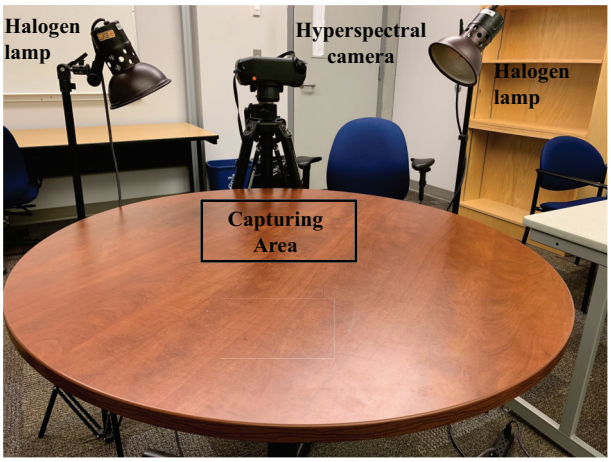

Figure 7: The experimental setup used to capture hyperspectral images of hands and arms of human subjects.

Figure 8: RGB samples from the collected dataset. Images shown are the RGB rendering captured by the hyperspectral sensor containing 3 visible bands.

for processing. The Specim IQ camera comes with a software tool to visualize hyperspectral images.

Human Subjects and Data Collection. The goal of our experiments is to show the effectiveness of our method in visualizing veins in human subjects. Since our experiments involve humans, and despite the minimal risk to them, we had to secure the approval of the Research Ethics Board at our university, which we did.

We recruited 13 subjects (9 males and 4 females). The subjects were informed about the purpose of the research and asked for their permission before conducting experiments, according to the protocol approved by the Research Ethics Board. The subjects also agreed to anonymously share the collected data for research purposes. We asked the subjects to put their hands (front and back) and forearms over the experimental table. We captured 16 hyperspectral images of each subject. Each image has 204 spectral bands, and each band has a spatial resolution of 512×512. We captured images in different positions, including front and back of palm, wrist, and upper and lower arm. RGB renderings of sample images of the captured data are shown in Figure 8.

In total, we captured 214 hyperspectral images, each with 204 bands. In addition, each hyperspectral image has a corresponding RGB image, which has three bands (R, G, B) in the visible range of the spectrum.

After capturing, the data is transferred form the camera to the workstation for processing and error checking. We used Matlab to extract all 204 bands from each hyperspectral image. Some error checks are performed after extracting hyperspectral data, e.g., sensor values should be within the range $(0 - 4095)$. We removed 7 corrupted images.

As mentioned before, the near infrared range $820 - 920nm$ can be used to visualize human veins and differentiate them from regular skin tissues. Our hyperspectral camera captures 34 bands in this range. We use all 34 bands in training and testing our deep neural network model. Therefore, our hyperspectral image dataset for vein visualization has a total of $34 \times 207 = 7,038$ images, in addition to the corresponding RGB images. We make this dataset public at [10].

Model Implementation and Training. To train and test our deep neural network model, we divide the collected data in two parts: (i) 75% of the data for training and (ii) 25% of the data for validation and testing. In addition, to stress the robustness of the model, the data used in validation and testing comes from different human subjects that were not seen during training. Specifically, out of the 13 human subjects, we use the data of 10 subjects for training. The data of the other 3 subjects are used for validation

and testing. Furthermore, the data for one of these 3 subjects was captured under a different lighting condition, not present in the training dataset. Moreover, we use data augmentation techniques, e.g., rotation and flipping, to increase the training dataset by 8X.

In summary, we created the following datasets:

- Training Dataset: has a total of **42,976 samples**, each sample contains a pair of RGB image and one of the 34 hyperspectral bands in the range $[820 - 920nm]$. These samples come from 10 human subjects. After removing corrupted images, we have 158 hyperspectral images each with 34 bands, which were augmented 8X. Thus, the number of training samples is $158 \times 8 \times 34 = 42,976$.
- Validation Dataset: has a total of **850 samples** in the same format as the Training Dataset, but these samples come from 3 different human subjects. After removing corrupted images, we have 25 hyperspectral images each with 34 bands. No data augmentation is used for the Validation Dataset.
- Testing Dataset: has a total of **24 samples** having the same data distribution as the Validation Dataset. These samples are entirely different from the Validation samples, but come from the same 3 human subjects as used in Validation. Each RGB image has 34 bands as ground truth, but we use one band $850nm$ for comparison against the predicted band.

After we construct the datasets, we train the model using two approaches: with and without white balancing. We refer to the first as HS_1, where the subscript indicates that we are reconstructing one hyperspectral band. We refer to the second model as $HS_1 - wb$, where '–' indicates without white balancing.

The proposed neural network is trained using 50×50 image patches having a stride of 50. The batch size is set to 64 and the Adam [21] optimizer is used by setting $\beta_1 = 0.9$, $\beta_2 = 0.999$, and $\epsilon = 10^{-8}$. The initial learning rate is 10^{-4} with the polynomial function as the decay policy. We have used $power = 1.5$ empirically for training efficiently. The model is implemented in PyTorch and trained on an NVIDIA TITAN RTX GPU with 24 GB memory.

4.2 Performance Metrics

We evaluate the performance of the proposed method using the following metrics.

- *Mean Relative Absolute Error (MRAE)*: This metric measures the relative absolute error between the reconstructed and ground truth hyperspectral images. We measure *MRAE* to analyse the quality of reconstruction.
- *Relative Root Mean Square Error (RMSE)*: This metric measures the second order relative error between the reconstructed and ground truth hyperspectral images. The *RMSE* is defined as:

$$RMSE = \sqrt{\frac{1}{N}\sum_{i,b}(I^R_{i,b} - I^G_{i,b}/I^G_{i,b})^2}, \tag{5}$$

  where $I^R_{i,b}$ and $I^G_{i,b}$ denote the i^{th} pixel in band b of the reconstructed and ground truth hyperspectral image, respectively, and N is the total number of pixels. We measure *RMSE* to get the average relative error estimate of the recontruction.
- *Coefficient of Correlation (CoC)*: This metric provides the proximity measure between the reconstructed image with respect to the ground truth image. The Pearson product-moment correlation coefficient is invariant to linear transformations and insensitive to uniform variations in brightness or contrast across an image. The *CoC* is defined as:

$$CoC = \frac{\sum_{i,b}(I^R_{i,b} - \bar{I}^R_{i,b})(I^G_{i,b} - \bar{I}^G_{i,b})}{\sqrt{(\sum_{i,b}[I^R_{i,b} - \bar{I}^R_{i,b}]^2)(\sum_{i,b}[I^G_{i,b} - \bar{I}^G_{i,b}]^2)}}, \tag{6}$$

  where $I^R_{i,b}$ and $I^G_{i,b}$ denote the i^{th} pixel in band b of the reconstructed and ground truth hyperspectral images, respectively, and $\bar{I}^R_{i,b}$ is the mean of $I^R_{i,b}$. We measure *CoC* because it is generally used in vein pattern matching in many authentication systems.
- *Structural Similarity Index (SSIM)*: This metric measures the quality of a reconstructed image relative to the ground truth hyperspectral image. We measure *SSIM* because it uses perceptual models that simulate the Human Visual System.

4.3 Visual Results

To evaluate the perceptual quality of hyperspectral reconstruction, we show sample results in Figure 9. The reconstructed results corresponding to the models HS_1 and $HS_1 - wb$ are evaluated on the same test samples. The intensity values of reconstructed results are analysed in the reconstructed band compared to the ground truth. As can be seen, the difference in intensity values recovered is small compared to the ground truth. The vein structure visible in the reconstructed result is similar to that present in ground truth.

We further analyse the reconstruction produced by the HS_1 model by plotting the absolute error map with respect to the ground truth. The results are shown in Figure 10. The reconstructed band and the ground truth band ($850nm$) have values in the range $0 - 4095$. So, we calculate the normalized error difference by using the formula $(GT - HS_1)/4095$, where GT is the ground truth and HS_1 is the reconstructed band. The error resulting from the reconstructed band produced by our model is very small and lies in the range $[0 - 0.1]$. If we were to plot a standard colormap in the range of $0 - 1$, we would hardly see anything in the error map, as the distribution of error values will be over a very small color region. Instead, we focus on the small error range of $[0 - 0.1]$ and plot the error map in this range. Darker regions (red-black) correspond to relatively higher errors, whereas lighter regions (white-yellow) correspond to lower errors, but all are in the small error $[0 - 0.1]$ range. In Figure 10, the black/dark red color is showing high error with respect to different part of the image, but it is still less than 0.1. The low error also shows that our model is able to learn the correct positions of the vein and not trying to produce artificial veins randomly.

For further validation of the accuracy of the produced results, the recovered intensities corresponding to veins and normal skin are analysed in the spatial domain. We compare the recovered intensities of the reconstructed band with the ground truth as shown in Figure 11. The intensities are plotted against a chosen spatial position marked by the red line in the left image. The intensity values reconstructed by the HS_1 model are compared against the ground truth (GT). The positions of the localized veins marked (blue dot) in the left image correspond to the vertical blue dotted

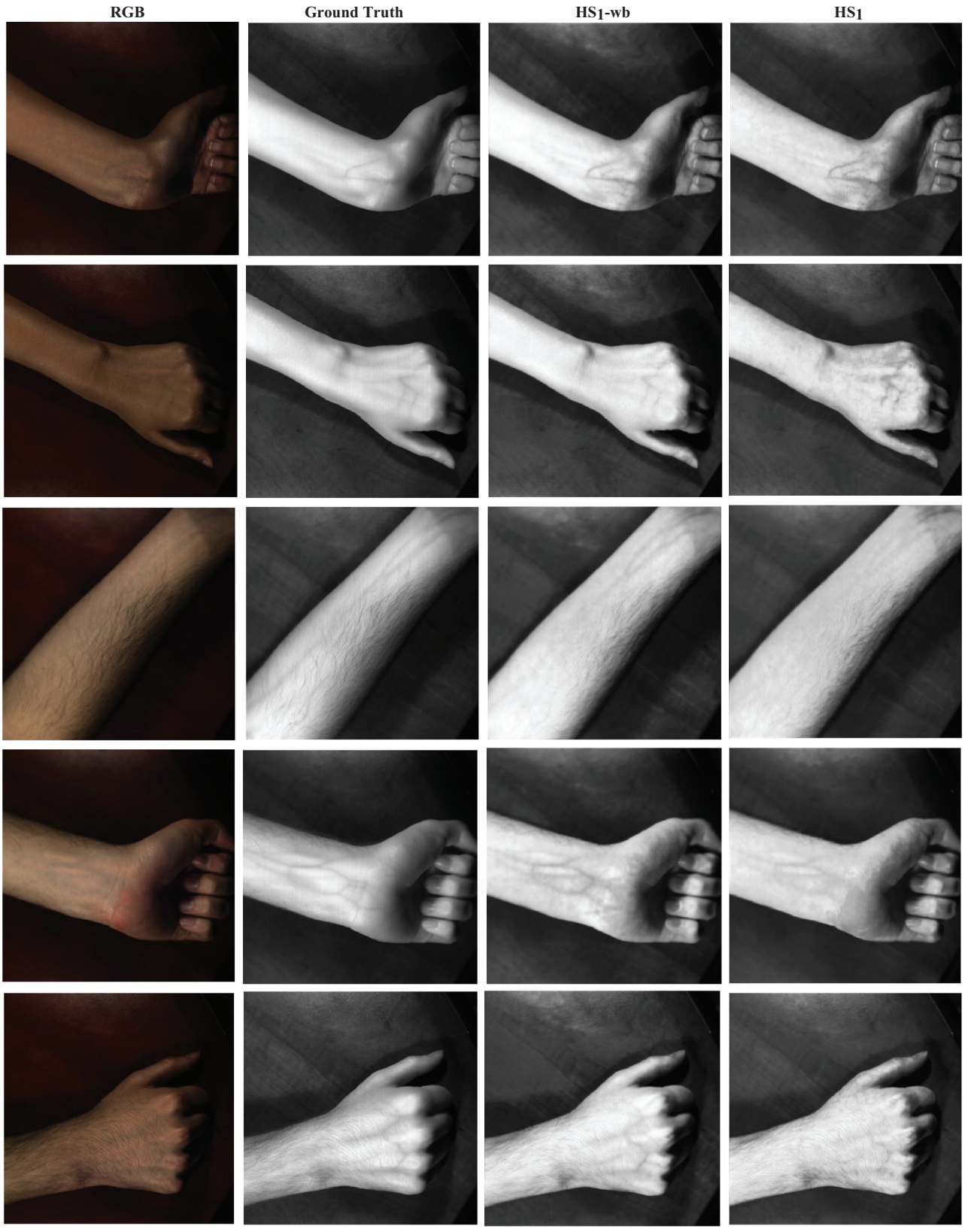

Figure 9: Comparing the reconstructed hyperspectral images using our model (rightmost column, denoted by HS_1) versus the ground truth captured by a hyperspectral camera (second column). The first column shows the RGB images, and the third column shows the reconstructed hyperspectral images produced by our model but without using white balancing (denoted by $HS_1 - wb$).

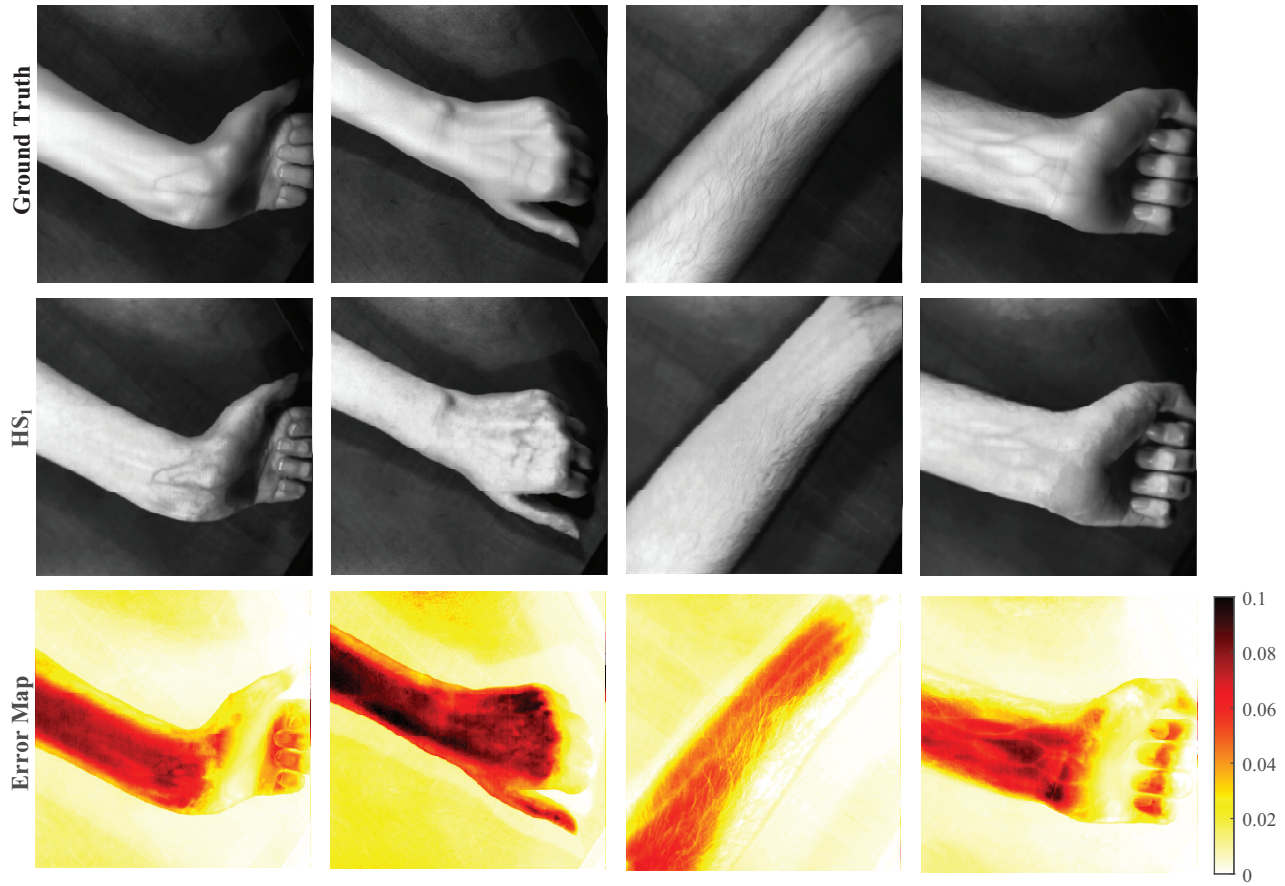

Figure 10: Analysing the accuracy of the reconstructed hyperspectral images (second row) relative to the ground truth images (first row) using error maps (third row). Notice that the range for the error maps is only $[0 - 0.1]$ instead of the standard range $[0 - 1]$, since the resulting error of our method is very small and will not be seen on a standard error map. Darker regions indicate larger errors.

lines in the plot on the right. The curves plotted in the right part of Figure 11 indicate that the recovered intensities are near to the ground truth ones, which shows the accuracy of our reconstruction method for vein localization.

4.4 Quantitative Analysis

We compute all performance metrics described in Section 4.2 using the Testing Dataset. The performance results are summarized in Table 1, which shows that the proposed model (HS_1) yields low error rates in terms of the MRAE and RMSE metrics (values close to 0 are better). The model also produces high accuracy in terms of the CoC and SSIM metrics (values close to 1.0 are better).

As mentioned earlier, our Testing Dataset consists of images taken in different illuminations, where some of the images have similar illumination as in the Training Dataset while others have illumination that does not exist in the Training Dataset. We evaluate the impact of white balancing on the performance of our model. The results are also shown in Table 1, where $HS_1 - wb$ refers to our model without white balancing. The results show that HS_1 produces lower error rates in terms of MRAE and RMSE metrics

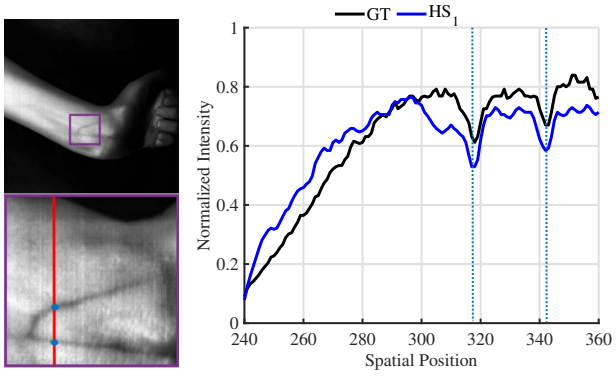

Figure 11: Spatial intensities plotted along the red line in the lower left image. Recovered intensities using reconstruction model HS_1 are compared to the ground truth (GT). The dotted vertical lines in the plot correspond to the specific vein positions marked with blue in the left image.

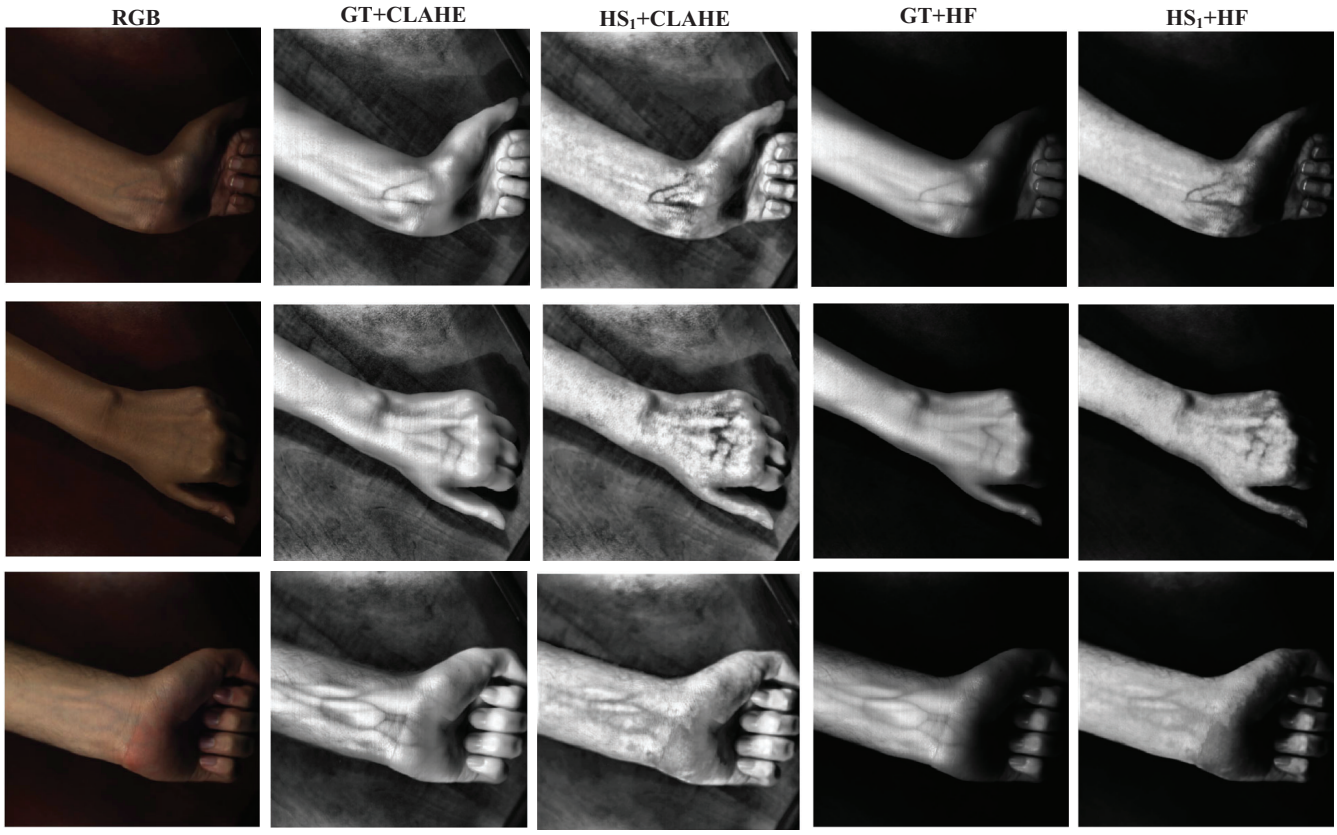

Figure 12: Vein image enhancements. First column shows RGB image, second and third column are the enhanced ground truth and the enhanced reconstructed band by applying Contrast Limited Adaptive Histogram Equalization (CLAHE). The last two columns are the enhanced ground truth and the enhanced reconstructed band by applying the homomorphic filtering (HF).

Table 1: The quantitative performance metrics produced by the proposed model with white balancing (HS_1) and without white balancing ($HS_1 - wb$). Bold font indicates the best performance.

Metric	$HS_1 - wb$	HS_1
MRAE	0.2200	**0.1541**
RMSE	0.2508	**0.1770**
CoC	0.9448	**0.9817**
SSIM	**0.9127**	0.9086

as well as higher accuracy in terms of the CoC metric. The SSIM metric produced by the HS_1 model, however, is slightly lower than that produced by $HS_1 - wb$ model. But it is still fairly high, more than 0.9, in both cases.

4.5 Enhancements for Vein Visualization

The vein enhancement methods, described in Section 3.3, are implemented in MATLAB. Image enhancements are applied on the gray scale image having vein information. We enhance the images by applying these techniques on the reconstructed band. We also perform the same operations on the ground truth band. Sample results are shown in Figure 12, where the first column shows the RGB image used as input to the reconstruction model HS_1. The second and third columns depict results obtained by applying CLAHE enhancement on the ground truth and the reconstructed band, respectively. Similarly, the last two columns depict results obtained by applying the Homomorphic filtering enhancement.

As Figure 12 shows, the image enhancement techniques produce better contrast and provide clearer visualization of the veins.

5 CONCLUSIONS AND FUTURE WORK

We proposed a data-driven method to reconstruct hyperspectral images from RGB ones. The method is based on a residual learning approach that is effective in capturing the structure of the data manifold, and takes into account the spatial contextual information present in RGB images for the spectral reconstruction process. The proposed RGB-to-hyperspectral conversion method handles images taken in different illuminations, which is an important feature for practical applications. The proposed method is general and can support various applications. To show the value of the proposed conversion method, we designed and evaluated a vein visualization application. We collected one of the first hyperspectral datasets in

this domain using a commercial hyperspectral camera; we make this dataset available for other researchers. We used this dataset to train our deep learning model and as ground truth for comparisons. Our experimental results show that the proposed method provides accurate vein visualization and localization results.

The work in this paper shows the potential of bringing some of the rich features of hyperspectral imaging to common RGB cameras, which can potentially enable many new image and video applications as well as improve the performance of existing ones. In the future, we plan to explore other applications that can benefit from hyperspectral imaging.

REFERENCES

[1] Farnaz Agahian, Seyed Ali Amirshahi, and Seyed Amirshahi. 2008. Reconstruction of reflectance spectra using weighted principal component analysis. *Color Research Application* 33 (October 2008), 360 – 371.

[2] Robert Allison, Joshua Johnston, Gregory Craig, and Sion Jennings. 2016. Airborne Optical and Thermal Remote Sensing for Wildfire Detection and Monitoring. *Sensors* 16, 8 (August 2016), 1310.

[3] Boaz Arad and Ohad Ben-Shahar. 2016. Sparse Recovery of Hyperspectral Signal from Natural RGB Images. In *European Conference on Computer Vision*. Springer, 19–34.

[4] Boaz Arad, Ohad Ben-Shahar, Radu Timofte, Luc Van Gool, Lei Zhang, and Ming-Hsuan Yang. 2018. NTIRE 2018 Challenge on Spectral Reconstruction from RGB Images. In *Proceedings of the IEEE/CVF Conference on Computer Vision and Pattern Recognition Workshops (CVPRW)*. 1042–104209.

[5] Yahia Ayoub, Sameer Serhal, Baraa Farhat, Ali Ali, Jason Amatoury, Hassan Nasser, and Mohamad Abou Ali. 2018. Diagnostic Superficial Vein Scanner. In *Proceedings of the IEEE International Conference on Computer and Applications (ICCA)*. 321–325.

[6] A. M. R. R. Bandara, K. A. S. H. K. Rajarata, and P. W. G. R. M. P. B. Giragama. 2017. Super-efficient spatially adaptive contrast enhancement algorithm for superficial vein imaging. In *Proceedings of the IEEE International Conference on Industrial and Information Systems (ICIIS)*. 1–6.

[7] Marjan Barakzehi, Seyed Amirshahi, Shahram Peyvandi, and Mansoureh ghanbar afjeh. 2013. Reconstruction of total radiance spectra of fluorescent samples by means of nonlinear principal component analysis. *Journal of the Optical Society of America. A, Optics, image science, and vision* 30 (September 2013), 1862–70.

[8] Frodo Kin Sun Chan, Xiaojie Li, and Adams Wai-Kin Kong. 2017. A Study of Distinctiveness of Skin Texture for Forensic Applications Through Comparison With Blood Vessels. *In IEEE Transactions on Information Forensics and Security* 12, 8 (August 2017), 1900–1915.

[9] Source Code. 2020. https://github.com/nehasharma512/vein-visualization

[10] Dataset. 2020. https://nsl.cs.sfu.ca/projects/hyperspectral/hyperspectral_data/dataset.zip.

[11] Chao Dong, Chen Change Loy, Kaiming He, and Xiaoou Tang. 2016. Image Super-Resolution Using Deep Convolutional Networks. *IEEE Transactions on Pattern Analysis and Machine Intelligence* 38, 2 (Feb. 2016), 295–307.

[12] Niloofar Eslahi, Seyed Hossein Amirshahi, and Farnaz Agahian. 2009. Recovery of spectral data using weighted canonical correlation regression. *Optical Review* 16, 3 (01 May 2009), 296–303.

[13] Brooks Ficke, Erin Ransom, and Jean Oakes. 2017. Near-Infrared Vein Visualization in Index Finger Pollicization. *The Journal of Hand Surgery* 42 (April 2017).

[14] Graham Finlayson and Elisabetta Trezzi. 2004. Shades of Gray and Colour Constancy. *Proceedings of the Color Imaging Conference*, 37–41.

[15] Mayank Goel, Eric Whitmire, Alex Mariakakis, T. Scott Saponas, Neel Joshi, Dan Morris, Brian Guenter, Marcel Gavriliu, Gaetano Borriello, and Shwetak N. Patel. 2015. HyperCam: Hyperspectral Imaging for Ubiquitous Computing Applications. In *Proceedings of the ACM International Joint Conference on Pervasive and Ubiquitous Computing (UbiComp '15)*. Association for Computing Machinery, New York, NY, USA, 145–156.

[16] Kaiming He, Xiangyu Zhang, Shaoqing Ren, and Jian Sun. 2016. Deep Residual Learning for Image Recognition. In *Proceedings of the IEEE Conference on Computer Vision and Pattern Recognition (CVPR)*. 770–778.

[17] Sergey Ioffe and Christian Szegedy. 2015. Batch Normalization: Accelerating Deep Network Training by Reducing Internal Covariate Shift. In *Proceedings of the International Conference on International Conference on Machine Learning (ICML'15)*, Vol. 37. 448–456.

[18] Muhammad Jaleed Khan, Hamid Saeed Khan, Adeel Yousaf, Khurram Khurshid, and Asad Abbas. 2018. Modern Trends in Hyperspectral Image Analysis: A Review. *IEEE Access* 6 (2018), 14118–14129.

[19] Jiwon Kim, Jung Kwon Lee, and Kyoung Mu Lee. 2016. Accurate Image Super-Resolution Using Very Deep Convolutional Networks. In *Proceedings of the IEEE Conference on Computer Vision and Pattern Recognition (CVPR)*. 1646–1654.

[20] Sewoong Kim, Dongrae Cho, Jihun Kim, Manjae Kim, Sangyeon Youn, Jae Eun Jang, Minkyu Je, Dong Hun Lee, Boreom Lee, Daniel L. Farkas, and Jae Youn Hwang. 2016. Smartphone-based multispectral imaging: system development and potential for mobile skin diagnosis. *Biomedical Optics Express* 7, 12 (December 2016), 5294–5307.

[21] Diederik P. Kingma and Jimmy Ba. 2014. Adam: A Method for Stochastic Optimization. arXiv:cs.LG/1412.6980

[22] Huiqun Li, Zhiwei Xiong, Zhan Shi, Lizhi Wang, Dong Liu, and Feng Wu. 2018. HSVCNN: CNN-Based Hyperspectral Reconstruction from RGB Videos. In *Proceedings of the IEEE International Conference on Image Processing (ICIP)*. 3323–3327.

[23] Tim Maecken and Thomas Grau. 2007. Ultrasound imaging in vascular access. *Critical Care Medicine* 35 (June 2007), S178–85.

[24] Meeshawn Marathe, Nayan S. Bhatt, and Raji Sundararajan. 2014. A novel wireless vein finder. In *Proceedings of the International Conference on Circuits, Communication, Control and Computing*. 277–280.

[25] Farhad Moghareh Abed, Seyed Amirshahi, and Mohammad Abed. 2009. Reconstruction of reflectance data using an interpolation technique. *Journal of the Optical Society of America. A, Optics, image science, and vision* 26 (April 2009), 613–24.

[26] Vinod Nair and Geoffrey E. Hinton. 2010. Rectified Linear Units Improve Restricted Boltzmann Machines. In *Proceedings of the International Conference on International Conference on Machine Learning (ICML'10)*. Omnipress, USA, 807–814.

[27] Rang M. H. Nguyen, Dilip K. Prasad, and Michael S. Brown. 2014. Training-Based Spectral Reconstruction from a Single RGB Image. In *Computer Vision – ECCV 2014*. 186–201.

[28] Jinsung Oh and Heesoo Hwang. 2010. Feature enhancement of medical images using morphology-based homomorphic filter and differential evolution algorithm. *International Journal of Control, Automation and Systems* 8, 4 (01 August 2010), 857–861.

[29] Seoung Wug Oh, Michael S. Brown, Marc Pollefeys, and Seon Joo Kim. 2016. Do It Yourself Hyperspectral Imaging with Everyday Digital Cameras. In *Proceedings of the IEEE Conference on Computer Vision and Pattern Recognition (CVPR)*. 2461–2469.

[30] Cheng-Tang Pan, Mark Francisco, Yen Chung kun, Shao-Yu Wang, and Yow-Ling Shiue. 2019. Vein Pattern Locating Technology for Cannulation: A Review of the Low-Cost Vein Finder Prototypes Utilizing near Infrared (NIR) Light to Improve Peripheral Subcutaneous Vein Selection for Phlebotomy. *Sensors* 19 (August 2019), 3573.

[31] Zhan Shi, Chang Chen, Zhiwei Xiong, and Dong Liu. 2018. HSCNN+: Advanced CNN-Based Hyperspectral Recovery from RGB Images. In *Proceedings of the IEEE/CVF Conference on Computer Vision and Pattern Recognition Workshops (CVPRW)*. 1052–10528.

[32] Jae Hee Song, Choye Kim, and Yangmo Yoo. 2015. Vein Visualization Using a Smart Phone With Multispectral Wiener Estimation for Point-of-Care Applications. *IEEE Journal of Biomedical and Health Informatics* 19, 2 (March 2015), 773–778.

[33] S. Sravani, Sumbul Naqvi, N. Sriraam, Manam Mansoor, Imran Badshah, Mohammed Saleem, and G. Kumaravelu. 2013. Portable Subcutaneous Vein Imaging System. *International Journal of Biomedical and Clinical Engineering* 2 (June 2013), 11–22.

[34] Tsuyoshi Takatani, Takahito Aoto, and Yasuhiro Mukaigawa. 2017. One-Shot Hyperspectral Imaging Using Faced Reflectors. In *Proceedings of the IEEE Conference on Computer Vision and Pattern Recognition (CVPR)*. 2692–2700.

[35] Soheil Varastehpour, Hamid Sharifzadeh, Iman Ardekani, and Xavier Francis. 2019. Vein Pattern Visualisation and Feature Extraction using Sparse Auto-Encoder for Forensic Purposes. In *Proceedings of the IEEE International Conference on Advanced Video and Signal Based Surveillance (AVSS)*. 1–8.

[36] Zhiwei Xiong, Zhan Shi, Huiqun Li, Lizhi Wang, Dong Liu, and Feng Wu. 2017. HSCNN: CNN-Based Hyperspectral Image Recovery from Spectrally Undersampled Projections. In *Proceedings of the IEEE International Conference on Computer Vision Workshops (ICCVW)*. 518–525.

[37] Emre Yaprak and Sibel Kayaalti-Yuksek. 2017. Preliminary evaluation of near-infrared vein visualization technology in the screening of palatal blood vessels. *Medicina Oral Patología Oral y Cirugia Bucal* 23 (December 2017).

[38] Herbert D. Zeman, Gunnar Lovhoiden, and Carlos Vrancken. 2005. Prototype vein contrast enhancer. *Optical Engineering* 44, 8 (2005), 1 – 9.

[39] Vladimir P. Zharov, Scott Ferguson, John F. Eidt, Paul C. Howard, Louis M. Fink, and Milton Waner. 2004. Infrared imaging of subcutaneous veins. *Lasers in Surgery and Medicine* 34, 1 (2004), 56–61.